Probing the Evolutionary History of Comets: An Investigation of the Hypervolatiles CO, CH_4, and C_2H_6 in the Jupiter-family Comet 21P/Giacobini-Zinner

Proposed running head: Hypervolatiles in 21P/Giacobini-Zinner

Nathan X. Roth[1,2,12], Erika L. Gibb[1,3,12], Boncho P. Bonev[4,12], Michael A. DiSanti[3,5,12], Neil Dello Russo[6,12], Adam J. McKay[4,5,12], Ronald J. Vervack, Jr.[6,12], Hideyo Kawakita[7,12], Mohammad Saki[1,12], Nicolas Biver[8,12], Dominique Bockelée-Morvan[8,12], Lori Feaga[9,12], Nicolas Fougere[10,12], Anita Cochran[11,12], Michael Combi[10,12], and Yinsi Shou[10,12]

[1]Department of Physics & Astronomy, University of Missouri-St. Louis, One University Blvd., St. Louis, MO, USA

[2]Solar System Exploration Division, Astrochemistry Laboratory Code 691, NASA-Goddard Space Flight Center, Greenbelt, MD, USA

[3]Goddard Center for Astrobiology, NASA-Goddard Space Flight Center, Greenbelt, MD, USA

[4]Department of Physics, American University, Washington, DC, USA

[5]Solar System Exploration Division, Planetary System Laboratory Code 693, NASA-Goddard Space Flight Center, Greenbelt, MD, USA

[6]Johns Hopkins Applied Physics Laboratory, Laurel, MD, USA

[7]Koyoma Astronomical Observatory, Kyoto Sangyo University Motoyama, Kamingamo, Kita-ku, Kyoto 603-8555, Japan

[8]LESIA, Observatoire de Paris, PSL Research University, CNRS, Sorbonne Université, Université de Paris, Sorbonne Paris Cité, Meudon, France

[9]Department of Astronomy, University of Maryland, College Park, MD, USA

[10]Department of Climate and Space Sciences and Engineering, University of Michigan, Ann Arbor, Michigan, USA

[11]McDonald Observatory, University of Texas at Austin, Austin, TX, USA

[12]Visiting Astronomer at the Infrared Telescope Facility, which is operated by the University of Hawaii under contract NNH14CK55B with the National Aeronautics and Space Administration

Submitted to Astronomical Journal May 20, 2019

Editorial correspondence and proofs should be directed to NXR

Nathan X. Roth

8800 Greenbelt Road

Greenbelt, MD 20771

Phone: 301-286-8151

E-mail: nathaniel.x.roth@nasa.gov

ABSTRACT

Understanding the cosmogonic record encoded in the parent volatiles stored in cometary nuclei requires investigating whether evolution (thermal or otherwise) has modified the composition of short-period comets during successive perihelion passages. As the most volatile molecules systematically observed in comets, the abundances of CO, CH_4, and C_2H_6 in short-period comets may serve to elucidate the interplay between natal conditions and post-formative evolution in setting present-day composition, yet secure measurements of CO and CH_4 in Jupiter-family comets (JFCs) are especially sparse. The highly favorable 2018 apparition of JFC 21P/Giacobini-Zinner enabled a sensitive search for these "hypervolatiles" in a prototypical carbon-chain depleted comet. We observed 21P/Giacobini-Zinner with the iSHELL spectrograph at the NASA Infrared Telescope Facility on four pre-perihelion dates, two dates near perihelion, and one post-perihelion date. We obtained detections of CO, CH_4, and C_2H_6 simultaneously with H_2O on multiple dates. We present rotational temperatures, production rates, and mixing ratios. Combined with previous work, our results may indicate that the hypervolatile coma composition of 21P/Giacobini-Zinner was variable across apparitions as well as within a particular perihelion passage, yet the spread in these measurements is a fraction of the variation in each molecule from comet-to-comet. We discuss the implications of our measured hypervolatile content of 21P/Giacobini-Zinner for the evolution of JFCs, and place our results in the context of findings from the Rosetta mission and ground-based studies of comets.

1. INTRODUCTION

Comets are among the most primitive remnants of the solar system's formation. They accreted in the early stages of the protosolar nebula and have been stored for the last ~4.5 Gyr in the cold outer solar system in the scattered Kuiper disk or in the Oort cloud dynamical reservoirs. Because comets lack a known mechanism for efficient internal self-heating owing to their small sizes, the present-day volatile composition of their nuclei likely reflects to a large degree the composition and conditions where (and when) they formed. Thus, measuring the volatile composition of comets offers an opportunity to place observational constraints on the history of the early solar system by measuring the abundances of trace species in their nuclei (Mumma and Charnley 2011, Bockelée-Morvan et al. 2004).

The volatile inventory of comets can be inferred by studying their coma composition during passages into the inner solar system (heliocentric distance $R_h \leq 3$ au). Such studies at multiple wavelengths have revealed extensive chemical diversity among the comet population (e.g., A'Hearn et al. 1995, Crovisier et al. 2009, A'Hearn et al. 2012, Cochran et al. 2012, Ootsubo et al. 2012, Dello Russo et al. 2016). In particular, high-resolution near-infrared spectroscopy provides a valuable tool for sampling the composition of primary volatiles (i.e., ices subliming directly from the nucleus) of comets via analysis of fluorescence emission in cometary comae. To date, over 30 comets have been characterized in this manner, with the hypothesis that the primary volatile composition of the coma can be used to infer the composition of the nucleus, and can therefore be tied to nascent solar system conditions.

However, the results of recent rendezvous missions to comets, such as the Rosetta mission to comet 67P/Churyumov-Gerasimenko, have raised significant questions regarding the nature of comets. These include questions such as: How did comets form? How are comet ices put together? How do comets change with time? To what degree do comets retain cosmogonic

signatures in their nuclei? How does coma composition vary throughout a perihelion passage? (see A'Hearn 2017 for a discussion of these questions). Whereas Oort cloud comets (OCCs) can generally be observed only during a single apparition, short-period (or ecliptic) comets, primarily Jupiter-family comets (JFCs), offer the opportunity to investigate potential evolutionary effects on volatile composition due to frequent and repeated perihelion passages, as well as a search for variability in coma composition on a variety of timescales (e.g., Knight & Schleicher 2013, Combi et al. 2019) depending on observational opportunities. Most processes that may alter the properties of the nucleus are expected to affect a thin (at most a few meters deep) layer near the surface, which is likely lost over the course of a typical perihelion passage (see Stern et al. 2003). Nonetheless, an ecliptic comet that experiences many perihelion passages, particularly at small R_h, may (potentially) experience considerable processing compared to an OCC. Indeed, measured JFCs are on average depleted in certain primary volatiles, such as C_2H_2 and C_2H_6, relative to OCCs (Dello Russo et al. 2016). Understanding these potential evolutionary (or, natally inherent) effects, including observed differences between JFCs and OCCs, is essential for placing the results of coma composition studies into a meaningful context in the framework of solar system formation.

As the most volatile molecules systematically observed in comets, the "hypervolatiles" CO, CH_4, and C_2H_6 may be the most sensitive to both primordial conditions as well as thermal processing in comets (Dello Russo et al. 2016), and characterizing each molecule in an individual ecliptic comet may provide unique insights into its evolutionary history. Being symmetric hydrocarbons, CH_4 and C_2H_6 can only be sampled in the near-infrared due to their lack of a dipole moment and thus lack of allowed rotational modes. Of these molecules, detection of C_2H_6 has been reported in ten ecliptic comets to date. Whereas CO is readily

detectable at radio wavelengths and has been measured in several ecliptic comets (Crovisier et al. 2009), near-infrared measurements of CO and CH_4 in such comets are more elusive. The reason for this is that measuring near-infrared transitions of CO and CH_4 requires sufficiently large geocentric velocities (Δ_{dot}) to Doppler shift cometary emission lines away from their corresponding highly opaque telluric counterparts and into regions of adequate atmospheric transmittance. However, the overall lower gas production rates and hence fainter nature of JFCs (compared with OCCs) means that most observations traditionally take place near closest approach to Earth, coinciding with insufficient Δ_{dot} to measure their emission lines from CO and (especially) CH_4. This results in a paucity of complete hypervolatile inventories for JFCs (e.g., see Dello Russo et al. 2016).

Fortunately, the increased sensitivity and long on-source integration times afforded by the high-resolution iSHELL spectrograph, which became available for use at the NASA Infrared Telescope Facility (IRTF) in late 2016, together with unusually favorable apparitions for several short-period comets have to date enabled sensitive searches for these molecules in short-period comets 2P/Encke (Roth et al. 2018) and JFC 45P/Honda-Mrkos-Pajdušáková (DiSanti et al. 2017). The highly favorable 2018 perihelion passage of JFC 21P/Giacobini-Zinner (hereafter G-Z) featured sufficiently high geocentric velocity simultaneously with small geocentric distance, and afforded the opportunity to characterize its hypervolatile content. G-Z is the prototype for the eponymous "GZ-type" of carbon-chain depleted comets, depleted in both C_2 and NH_2 with respect to H_2O and accounting for ~6% of comets measured (A'Hearn et al. 1995, Fink 2009). Coupled with published near-infrared observations of G-Z during the 1998 and 2005 apparitions (Weaver et al. 1999, Mumma et al. 2000, DiSanti et al. 2013), our measurements also enabled searches for coma compositional variability of hypervolatiles on timescales of days, both pre- vs.

post-perihelion, and across multiple perihelion passages. In Section 2, we discuss our observations and data analysis. In Sections 3 and 4, we present our results. In Section 5, we compare our results to those from previous perihelion passages. In Section 6, we examine G-Z's place in the context of other comets characterized to date.

2. OBSERVATIONS AND DATA REDUCTION

During its 2018 apparition, G-Z both reached perihelion (1.01 au) and was closest to Earth (0.39 au) on September 10. On UT 2018 July 25, 28, 29, and 31, September 7 and 11, and October 10, we observed G-Z with the high-resolution ($\lambda/\Delta\lambda \sim 40{,}000$), near-infrared, immersion-grating echelle spectrograph iSHELL (Rayner et al. 2012, 2016) at the 3-m NASA IRTF to characterize its hypervolatile composition. We utilized three iSHELL settings (Lcustom, Lp1, and M2) so as to fully sample a suite of molecular abundances. We oriented the slit along the projected Sun-comet line on all dates (see Table 1).

On our July and October dates, observations were performed with a 6-pixel (0.75″) wide slit, using our standard ABBA nod pattern, with A and B beams symmetrically placed about the midpoint along the 15″ long slit and separated by half its length. A malfunction of the iSHELL dekker precluded the use of the 15″ long slit in September and necessitated off-chip nodding using the 0.75″ wide by 5″ long slit. We placed G-Z in the center of the slit for A frames and nodded 20″ perpendicular to the slit for B (sky) frames. Combining spectra of the nodded beams as A-B-B+A cancelled emissions from thermal background, instrumental biases, and "sky" emission (lines and continuum) to second order in air mass. Flux calibration was performed using appropriately placed bright IR flux standard stars on each date using a wide (4.0″) slit. **On October 10, observing time lost owing to a telescope pointing error precluded the acquisition of flux calibration sets; therefore, we adopted a flux calibration factor (Γ,**

W/m^2/cm^{-1}/counts/s), based on that measured on other dates. Although this could affect absolute production rates, derived mixing ratios should be unaffected, as our targeted molecules were observed simultaneously or contemporaneously with water or OH prompt emission (OH*, a proxy for water production, see Bonev et al. 2006). The observing log is shown in Table 1.

[Insert Table 1 Here]

Our data reduction procedures have been rigorously tested and are described extensively in the refereed literature (Bonev 2005, DiSanti et al. 2006, Villanueva et al. 2009, Radeva et al. 2010, DiSanti et al. 2014), and their application to unique aspects of iSHELL spectra is detailed in §3.2 of DiSanti et al. (2017). Here we will only discuss aspects of the reduction of G-Z frames which differed from those previously reported.

Each echelle order within an iSHELL setting was processed individually as previously described, such that each row corresponded to a unique position along the slit, and each column to a unique wavelength. We found that spatially resampling using a third-order polynomial more completely removed the curvature in the spatial dimension from iSHELL frames, and so employed this in place of previously used second-order polynomial resampling (DiSanti et al. 2017). Spectra were extracted from the processed frames by summing signal over 15 rows, seven rows to each side of the nucleus, defined as the peak of dust emission in a given spectral order.

For our September observations (using the shorter 5″ slit), we found that the iSHELL flat lamp provided illumination of the chip that was not consistent with that of the sky. This introduced a curvature effect into our spectra, which we corrected by fitting and then subtracting a polynomial baseline (Fig. 1). This may have affected flux calibration and therefore the calculated absolute molecular production rates (*Q*'s) reported for our September dates. However, emissions from all molecules within each individual iSHELL setting are sampled

simultaneously, and therefore our derived mixing ratios should be unaffected. The general consistency of production rates and derived mixing ratios on both September dates suggests that any uncertainties introduced by this illumination offset were likely minimal.

[Insert Figure 1]

We determined contributions from continuum and gaseous emissions in our comet spectra as previously described (e.g., DiSanti et al. 2016), and illustrate the procedure in Figure 2. We convolved the fully resolved transmittance function to the resolving power of the data (~ 4.0 x 10^4) and scaled it to the level of the comet continuum. We then subtracted the modeled continuum to isolate cometary emission lines and compared synthetic models of fluorescence emission for each targeted species to observed line intensities.

[Insert Figure 2]

Nucleocentric (or "nucleus-centered") production rates (Q_{NC}) were determined using our well-documented formalism (Dello Russo et al. 1998, DiSanti et al. 2001, Bonev 2005, Villanueva et al. 2011a); see §3.2.2 of DiSanti et al. (2016) for further details. The Q_{NC} were multiplied by an appropriate growth factor (GF), determined using our *Q*-curve methodology (e.g., Dello Russo et al. 1998, DiSanti et al. 2001, Bonev 2005, Gibb et al. 2012), to establish total (or global) production rates (*Q*). This GF corrects for atmospheric seeing, which suppresses signal along lines of sight passing close to the nucleus due to the use of a narrow slit, as well as potential drift of the comet during an exposure sequence. Global production rates for all detected molecules are listed in Table 2. GFs were determined for both gas and dust when the signal-to-noise ratio (S/N) was sufficiently high (i.e., only for H_2O, CO, and C_2H_6). For September dates, the short 5″ slit precluded the use of *Q*-curves to calculate GFs. Therefore, we assumed a GF of 1.8, a value consistent with that obtained from our other dates (Table 2).

3. RESULTS

3.1 Spatial Profiles

For July dates, we were able to extract spatial profiles for H_2O, CO, and C_2H_6 emissions in G-Z (Fig. 3). Within uncertainty, this suggests that emission for all three species closely tracked that of the co-measured dust; therefore, on dates for which molecular GFs could not be well-constrained, we adopted that of dust co-measured within each setting when calculating production rates (Table 2).

[Insert Figure 3 Here]

3.2 Mixing Ratios of Volatile Species

3.2.1 Molecular Fluorescence Analysis

Synthetic models of fluorescence emission for each targeted species were compared to observed line intensities, after correcting each modeled line intensity (*g*-factor) for the monochromatic atmospheric transmittance at its Doppler-shifted wavelength (according to the geocentric velocity of the comet at the time of the observations). The *g*-factors used in synthetic fluorescence emission models in this study were generated with quantum mechanical models developed for CO (Paganini et al. 2013), CH_4 (Gibb et al. 2003), C_2H_6 (Villanueva et al. 2011b), and H_2O (Villanueva et al. 2012). A Levenberg-Marquardt nonlinear minimization technique (Villanueva et al. 2008) was used to fit fluorescence emission from all species simultaneously in each echelle order, allowing for high-precision results, even in spectrally crowded regions containing many spectral lines within a single instrumental resolution element. Production rates for each sampled species were determined from the appropriate fluorescence model at the rotational temperature of each molecule (§3.2.2).

3.2.2 Determination of Rotational Temperature

Rotational temperatures (T_{rot}) were determined using correlation and excitation analyses as described in Bonev (2005, pp. 53-65), Bonev et al. (2008), DiSanti et al. (2006), and Villanueva et al. (2008). In general, well-constrained rotational temperatures can be determined for individual species having intrinsically bright lines and for which a sufficiently broad range of excitation energies is sampled. Utilizing the large spectral grasp of iSHELL, in the case of H_2O we were able to sample dozens of strong lines simultaneously.

We found consistent rotational temperatures for multiple molecules on all dates (including H_2O). The T_{rot} for H_2O was well-constrained on September 7 (being 75 ± 3 K) and was consistent (within 1σ uncertainty) with that for C_2H_6 on September 11 (66^{+12}_{-9} K). Rotational temperatures for our July dates were also in formal agreement, being 64^{+15}_{-11} K for CO on July 28 and 48^{+19}_{-13} K for H_2O on July 29. We were unable to derive well-constrained rotational temperatures for any molecules on October 10. We calculated production rates and mixing ratios at T_{rot} = 48 K and 64 K for July dates and varied T_{rot} as a parameter for the October date, calculating production rates and mixing ratios for each molecule at representative values T_{rot} = 50 K, 60 K, and 70 K. In general, mixing ratios for a given species derived at each temperature are consistent with one another within 1σ uncertainty (Table 2).

[Insert Table 2 Here]

3.2.3 Secure Detections of Hypervolatiles

Our detections of CO, CH_4, and C_2H_6 in G-Z are particularly notable for two reasons: (1) They address the paucity of measurements of CO and CH_4 in ecliptic comets in general, and (2) The measurement of these hypervolatiles in an individual ecliptic comet across multiple perihelion passages, and on multiple dates during its 2018 apparition. Of all primary volatiles systematically measured in comets, these three molecules are most sensitive to thermal

processing, but as noted earlier, CO and CH_4 are also among the most difficult to sample from the ground due to lack of sensitivity and/or adequate geocentric velocity. G-Z's excellent geocentric velocity ($|\Delta_{dot}| > 13$ km s^{-1} pre-perihelion, $|\Delta_{dot}| > 11$ km s^{-1} post-perihelion) allowed firm detections of all three species. CO and CH_4 have been measured in fewer than ten ecliptic comets (with most detections being below the 5σ level), making our measurements in G-Z a critical component in establishing statistics for these species in ecliptic comets, and determining the importance of natal versus evolutionary effects on present cometary volatile composition. Figures 4(A)-(E) show clear CO, H_2O, CH_4, C_2H_6, and OH* emissions in G-Z superimposed on the cometary continuum during various portions of its 2018 perihelion passage.

[Insert Figures 4 A-E Here]

4. Coma Hypervolatile Composition Throughout the 2018 Perihelion Passage of G-Z

The 2018 apparition of G-Z provided an opportunity to conduct the first comprehensive comparison of hypervolatile abundances for a comet through three perihelion passages and also on multiple dates within a given perihelion passage, thereby allowing us to address pressing questions in cometary science. These include testing possible evolutionary effects on coma volatile composition, as well as searching for coma compositional variability on multiple timescales, including day-to-day, pre- vs. post-perihelion, and across perihelion passages. We discuss each of these topics in turn, and place G-Z in the context of other comets observed to date. Unless otherwise noted, all dates refer to the 2018 apparition.

4.1 CO

We found clear, simultaneously measured detections of CO and H_2O on multiple dates in G-Z (Figs. 2,4(A),4(D)) pre- as well as post-perihelion. The mixing ratio CO/H_2O was consistent on all pre-perihelion July dates within 1σ uncertainty (Table 2; see also Fig. 5) with a weighted

average abundance of 1.72 ± 0.12% for T_{rot} = 64 K. This was somewhat lower post-perihelion in October, 1.26 ± 0.23% for T_{rot} = 60 K, suggesting that CO/H_2O in G-Z may display pre- vs. post-perihelion asymmetry. However, given the uncertainty in T_{rot} in October, it is important to note that the range of possible October CO mixing ratios is in formal agreement with those from July (Table 2). These mixing ratios are depleted with respect to the mean for all comets measured to date at near-infrared wavelengths (5.2 ± 1.3%), but are consistent with the few measurements in ecliptic comets (Dello Russo et al. 2016, DiSanti et al. 2017, Roth et al. 2018, Dello Russo et al. 2019).

4.2 CH_4

CH_4 bears the distinction of being the most severely undersampled hypervolatile in ecliptic comets, having been firmly measured in only six to date (Dello Russo et al. 2016 and refs. therein, DiSanti et al. 2017, Roth et al. 2018, Dello Russo et al. 2019). Utilizing the large spectral grasp of iSHELL, we detected CH_4 in G-Z at the 4σ level on July 28, at >6σ on July 31, and derived a meaningful constraint on its mixing ratio on October 10 (see Fig. 4(B) and Table 2). This suggests that CH_4 may have been variable from day-to-day in G-Z. However, there are important caveats for our CH_4 study.

We were unable to derive a well-constrained rotational temperature for CH_4 owing to the small spread in excitation energies in the sampled lines (see §3.2.2, Fig. 4B). However, we found that calculated CH_4 production rates and mixing ratios showed a sensitive dependence on assumed T_{rot} (Table 2). Assuming T_{rot} = 48 K (from H_2O on July 29), pre-perihelion CH_4 mixing ratios in G-Z (0.63 ± 0.17% for July 28, 1.12 ± 0.26% for July 31) are consistent with mean values in measured OCCs (0.88 ± 0.10%), yet are enriched compared to the few measurements in JFCs. Adopting a higher T_{rot} (e.g., 64 K from CO on July 28) increases the degree of CH_4-

enrichment. Regardless of which T_{rot} we adopt, G-Z is not the first instance of a CH_4-enriched JFC, with similar mixing ratios reported in 45P/Honda-Mrkos-Pajdušáková (DiSanti et al. 2017, Dello Russo et al. 2019). Our (3σ) upper limit for October 10 is similarly sensitive to assumed T_{rot} (Table 2), but is consistent with our July measurements assuming $T_{rot} \geq 60$ K, a reasonable assumption given the rotational temperatures measured in July and September for other molecules at similar R_h.

Additionally, we were unable to extract spatial profiles for CH_4 emission due to low S/N along the slit; therefore, we assumed GFs measured from other species (or co-measured dust) within a given date for CH_4 in order to calculate global production rates. It is possible that CH_4 outgassing differed day-to-day from that for H_2O, CO, or co-measured dust and that the suggested variability may be due to our assumed GFs for CH_4. That being said, we did not find any unusual outgassing patterns among the other molecules or dust relative to one another in G-Z, so we expect our assumed GF for CH_4 to be reasonable.

Finally, OH* was weak in G-Z for our July and October dates, and was only firmly detected near perihelion in September. **We therefore calculated mixing ratios for CH_4 using $Q(H_2O)$ obtained from the M2 setting on the same date. We estimate the inter-setting calibration uncertainty to be ~10%, and have incorporated this into the reported uncertainty in our mixing ratios. Use of contemporaneously (but not simultaneously) measured $Q(H_2O)$ for CH_4 abundances in July and October may account for some of the spread in abundances from date to date. However, the formal agreement between $Q(H_2O)$ obtained from OH* (in Lp1) and H_2O (in Lcustom) on September 7 (Table 2) argues against both a systematic difference in retrieving water production rates in these two ways,**

and also against short-term variations in $Q(H_2O)$ in G-Z. Clearly, further measurements of G-Z are necessary to clarify the possible variability of its coma CH_4 content.

4.3 C_2H_6

Of all the hypervolatiles, C_2H_6 is the most routinely sampled in comets owing to its intrinsically strong near-infrared transitions and the availability of multiple emissions in regions of favorable telluric transmittance independent of Δ_{dot}. This enabled us to measure C_2H_6 mixing ratios on multiple dates during G-Z's 2018 apparition, including pre-perihelion, near perihelion, and post-perihelion. Similar to CO, we found C_2H_6 mixing ratios were consistent (within uncertainties) pre-perihelion (weighted average 0.24 ± 0.03% for T_{rot} = 64 K) and additionally near perihelion (weighted average 0.29 ± 0.02%). However, C_2H_6 was lower post-perihelion with mixing ratio 0.14 ± 0.03% (assuming T_{rot} = 60 K). Compared to ecliptic comets measured to date, pre-perihelion and near perihelion G-Z was consistent with the mean mixing ratio measured for C_2H_6 (0.34 ± 0.07%), but was depleted post-perihelion (and was severely depleted compared to the mean for all comets measured (0.55 ± 0.08%), including ecliptic comets). In the same manner as CH_4, the use of $Q(H_2O)$ from H_2O in the M2 setting rather than from OH* in the Lp1 setting to calculate C_2H_6 mixing ratios in July and October may have contributed to its suggested variability. Similarly, the use of assumed GFs for C_2H_6 on some of our dates may have introduced additional uncertainty into the mixing ratio C_2H_6/H_2O. However, we note that $Q(H_2O)$ was dramatically lower in October compared with both July and September, being closer to 2 x 10^{28} than to 3 x 10^{28} molecules s^{-1} (see Table 2), consistent with asymmetry in water production with respect to perihelion found by A'Hearn et al. (1995). This in turn could indicate distinct regions of the nucleus dominating the activity in G-Z at these times, and that its chemical

composition (at least in terms of CH_4/H_2O and C_2H_6/H_2O) may also be different on October 10 compared with our pre-/near-perihelion dates.

5. Comparison with Previous Perihelion Passages

5.1 Comparison with Previous Perihelion Passages of G-Z

G-Z is the only comet observed at near-infrared wavelengths during three different perihelion passages: 1998 (Weaver et al. 1999, Mumma et al. 2000), 2005 (DiSanti et al. 2013), and 2018 (this work), and is just the second comet to have a comprehensive comparison of hypervolatile abundances across apparitions (the other being 2P/Encke; see Roth et al. 2018, Radeva et al. 2010). Figure 5A shows our individual 2018 measurements of hypervolatile abundances in G-Z. Figures 5B shows our mean pre-, near-, and post-perihelion hypervolatile abundances together with those for G-Z from 1998 and 2005, and (for comparison) those for all measured comets. Table 3 gives a similar comparison numerically. Figure 5 and Table 3 suggest that each hypervolatile may display at least some degree of variability, whether across perihelion passages or during a particular apparition. We discuss each species in turn.

[Insert Figures 5A-B Here]

[Insert Table 3 Here]

5.1.1 CO

In the case of CO, our pre- and post-perihelion mixing ratios are consistent with (yet lower than) the upper limit from the 1998 apparition (using CSHELL) found by Weaver et al. (1999), but considerably lower than the mixing ratio reported by Mumma et al. (2000) from observations conducted approximately three weeks earlier. However, Mumma et al. did not detect H_2O, even though the strong line near 2151 cm^{-1} (as we show in Figs. 4A and 4D) was encompassed together with the CO R0 and R1 lines in the same CSHELL setting. Instead, their

value for CO/H_2O was inferred from the measured CO abundance relative to C_2H_6 (detected at the ~5σ confidence level), and an adopted (1.9σ) value for $Q(H_2O)$ based on residual flux at the Doppler-shifted frequency of the 2151 cm^{-1} line. In any case, results obtained to date suggest that the abundance ratio of CO in G-Z may display variability, both during a single apparition (as is also suggested by our 2018 measurements) and across multiple apparitions.

It is important to note that the 1998 measurements of G-Z with CSHELL – the small spectral grasp of which precluded measuring H_2O simultaneously with CH_4 or C_2H_6 – introduced uncertainties due to inter-setting calibration in addition to potential temporal variations in production rates. In contrast, the large spectral grasp of iSHELL enabled simultaneous measurements of all three hypervolatiles with either H_2O or OH* during the 2018 perihelion passage of G-Z.

In the context of preserving natal solar system signatures in the nucleus ices of JFCs, it is important to note the stark contrast of our CO measurements along with those reported by Weaver et al. compared to those of Mumma et al. The CO/H_2O mixing ratio inferred by Mumma et al. (10 ± 6%) would place G-Z as the only known CO-enriched JFC to date. If G-Z were indeed so enriched in CO, it would have profound implications for the origins and evolutionary processing history of JFCs. However, as mentioned previously this is based on an extremely tentative "detection" (<2σ) of H_2O. Nonetheless, our measurements do not support this conclusion, and instead indicate that G-Z has a CO abundance that is more similar to the few measurements in ecliptic comets and is depleted when compared to all comets measured.

5.1.2 CH_4

CH_4 has not been reported previously in G-Z – for both the 1998 and 2005 observations $|\Delta_{dot}| < 10$ km s^{-1}, thereby precluding its measure – and our results indicate that it may have been

variable on timescales of days to months in 2018. However, as previously noted, there are important caveats regarding its purported variability. In any case, our measurements indicate that G-Z is **consistent with to enriched** compared to the mean CH_4 abundance for all comets measured.

5.1.3 C_2H_6

Our C_2H_6 mixing ratios obtained pre-perihelion and near perihelion were consistent with that found by Mumma et al. (2000) **(~0.2% relative to H_2O; however, this mixing ratio suffers the same systematic uncertainty noted for CO/H_2O in §5.1.1),** but were significantly higher than the upper limit (<0.05-0.08%) reported by Weaver et al. (1999), and also the measurement from 2005 (0.14%, DiSanti et al. 2013). However, our post-perihelion measurement for C_2H_6 on October 10 was considerably lower (by approximately a factor of 2) than on earlier 2018 dates, yet consistent with the 2005 pre-perihelion value, suggesting possible short-term (i.e., "diurnal", perhaps associated with nucleus rotation, or seasonal, such as that seen by Rosetta at 67P/Churyumov-Gerasimenko; see §5.2) variability in its C_2H_6 abundance ratio when compared with our pre-perihelion results. It is important to note that the possible variability in C_2H_6 implied by our G-Z measurements (as well as those from previous perihelion passages) is small compared to the overall spread of C_2H_6 abundances in all comets measured (Fig. 5).

5.2 Discussion of Possible Variability of Coma Hypervolatile Abundances in G-Z

Combined with previous work, our results suggest that coma hypervolatile abundances in G-Z may be variable. At 67P/Churyumov-Gerasimenko, the Rosetta mission found that nucleus shape and the location of active areas, combined with seasonal and rotational illumination effects, resulted in coma compositional variability on a variety of timescales. Hässig et al. (2015)

found long-term variation in the coma abundances of CO and CO_2 due to seasonal illumination effects; furthermore, other species (such as CH_4) varied on shorter timescales, showing diurnal variations that differed from those of other volatiles, such as CO and C_2H_6 (Luspay-Kuti et al. 2015, Bockelée-Morvan et al. 2016, Fink et al. 2016). Similar effects may have contributed to the suggested coma hypervolatile variability in G-Z. Unfortunately, our ground-based measurements do not have sufficient spatial resolution to test this possibility.

To further examine the nature of the suggested variability in G-Z, we examined the evolution of molecular production for each species reported here during the 2018 apparition. Figure 6 shows the production rate of each species relative to perihelion (on September 10). Our measurements for all four species (H_2O, CO, CH_4, C_2H_6) are consistent with A'Hearn et al. (1995), who found that G-Z was more active pre-perihelion than post-perihelion. However, our results indicate that the relative asymmetry in molecular production is more pronounced for the trace species than for H_2O, which is reflected in their generally lower post-perihelion compared to pre-perihelion mixing ratios (Fig. 5, Table 3).

[Insert Figure 6 Here]

In order to test whether the possible variability indicated by our results is owing to the activity of H_2O vs. that of the trace species in G-Z, we compared the ratios CO/C_2H_6 from the 2018 perihelion passage. We found that CO/C_2H_6 was consistent within uncertainty pre- vs. post-perihelion, being 7.18 ± 2.14 on July 28, 8.82 ± 1.69 on July 31, and 8.75 ± 1.85 on October 10 (assuming T_{rot} = 64 K for July and 60 K for October). Combined with the results shown in Figures 5 and 6, this suggests that although CO and C_2H_6 were consistent relative to one another throughout the 2018 perihelion passage, their contributions to the volatile content of the coma

were not, as evidenced by their steeper variation about perihelion compared with the production rate of H_2O.

If the volatile composition of G-Z is indeed variable, it is not the first such comet reported in the literature. As the number of serial measurements (i.e., both within and across perihelion passages) of primary volatiles in comets increases, the number of reports of variability on multiple timescales has similarly increased (e.g., Dello Russo et al. 2019, Roth et al. 2018, Fink et al. 2016, DiSanti et al. 2016, McKay et al. 2015, Feaga et al. 2014, Bodewits et al. 2014), with explanations ranging from diurnal variations in outgassing, to seasonal illumination effects, to chemically heterogeneous nuclei. Understanding whether such variations are common or rare phenomena and how to account for them in our analysis is crucial to placing the results of present-day primary volatile measurements in cometary comae into the framework of solar system formation theories.

It is important to note that the variability suggested by the measurements in Table 3 cannot explain the variation in each molecule among comets revealed in measurements to date (Figure 5). If the range of volatile abundances observed among all comets can be reproduced by time-resolved observations of one comet, we could seriously question the extent to which chemical diversity among the population is cosmogonic. Alternatively, a comet such as G-Z, in which measurements over three perihelion passages suggest (with carefully explored caveats) that the abundances of CO/H_2O and C_2H_6/H_2O vary on scales much smaller than the comet-to-comet range, may serve as evidence that we are indeed sampling cosmogonic signatures in our present-day measurements of parent volatiles in short-period comets. Further unraveling the complex relationship between nascent solar system conditions and evolutionary processes in

comets clearly requires increasing the sample size of serial measurements in short-period comets, particularly observations targeting hypervolatiles.

6 Comparison to Comets as Measured at Near-Infrared Wavelengths

Comprehensive hypervolatile abundances have been securely measured in 19 OCCs to date, yet in only four ecliptic comets, including G-Z. This highlights that statistics for these species in ecliptic comets (particularly CO and CH_4) are far from being firmly established. Figure 7 shows relative hypervolatile abundances reported in all comets to date, including G-Z and measurements taken by Rosetta at 67P/Churyumov-Gerasimenko using ROSINA measurements of C_2H_6 (Le Roy et al. 2015), MIRO measurements of CO (Biver et al. 2019), and VIRTIS measurements of CH_4 (Bockelée-Morvan et al. 2016). The particularly low C_2H_6/CH_4 ratio in G-Z (points 22-23) is supported by observations at other wavelengths. Kiselev et al. (2000) reported a blueish linear polarization spectrum for continuum in G-Z at optical wavelengths, and suggested this was caused by the presence of organic grains (or large-sized complex organics). This implies that G-Z is depleted in simple organics, such as C_2H_6, but is enriched in more complex organics, which may indicate warmer conditions were present during the formation and subsequent evolution of G-Z's constituent ices. Our low measured C_2H_6/CH_4 supports this hypothesis, and together with the observed blueish polarization, may indicate that simple hydrocarbons were efficiently converted into more complex organics in the ices that were incorporated into the nucleus of G-Z.

[Insert Figure 7 Here]

It is apparent from Figure 7 that hypervolatile abundances among OCCs span a large range of values. Similarly, as the hypervolatile abundances of more ecliptic comets are completely characterized, it appears that they may span a similar range of CO/CH_4 and

C_2H_6/CH_4 as that observed among OCCs, from severely depleted (45P/ Honda-Mrkos-Pajdušáková #20 in Fig. 7; DiSanti et al. 2017) to near-mean values (2P/Encke, #10; Roth et al. 2018) to (possibly) enriched values in 67P (LeRoy et al. 2015, Bockelée-Morvan et al. 2016, Biver et al. 2019). It is important to note that comparisons between the in-situ measurements of Le Roy et al. (2015) and bulk coma measurements (e.g., this work, Bockelée-Morvan et al. 2016, Biver et al. 2019) are not straightforward, particularly given the differences in R_h between each set of measurements. **Additionally, differences in observational circumstances, techniques, and analysis must be kept in mind when comparing results from studies of different comets.**

The relative isolation of G-Z in Figure 7 further highlights the spread in hypervolatile abundances among ecliptic comets, reflecting its unique combination of CH_4 being consistent with the mean among OCCs versus the moderately depleted values for CO and C_2H_6. This underscores that much work remains in firmly characterizing the ranges of hypervolatile abundances in ecliptic comets and understanding their implications for placing such measurements into a meaningful context.

7. Summary of Results

We characterized the hypervolatile composition of the prototypical "GZ-type" comet 21P/Giacobini-Zinner with the powerful, recently commissioned iSHELL spectrograph at the NASA-IRTF on four pre-perihelion dates, two dates near perihelion, and one post-perihelion date. Combined with previous work, our results suggest that coma abundances of all three hypervolatiles (CO, CH_4, and C_2H_6) may be variable on several timescales, including day-to-day, pre- vs post-perihelion, and even across perihelion passages. However, as noted in §5, there are

important caveats to our study, and additional serial measurements of G-Z are needed to confirm possible variability in its coma hypervolatile content. In any case, our results suggest that:

1. Mixing ratios of CO were consistent (within uncertainty) day-to-day pre-perihelion, but were slightly lower post-perihelion. Our measurements are consistent with depleted values compared to the mean among measured comets, as well as with an upper limit reported from the 1998 perihelion passage (Weaver et al. 1999).
2. Our measurements of CH_4, the most severely underrepresented hypervolatile in studies of ecliptic comets, represent its first reported values in G-Z. CH_4 abundances were consistent with mean values among all comets measured, and may have been variable from day-to-day. However, there are important caveats to the possible variability of CH_4 in G-Z **(§4.2**, 5.2).
3. We found that the mixing ratio of C_2H_6 decreased significantly pre- vs. post-perihelion, its post-perihelion value being consistent with being strongly depleted. Our pre-perihelion C_2H_6 mixing ratios were enriched compared to measurements during the same seasonal phase in 2005 (DiSanti et al. 2013), yet our post-perihelion mixing ratio was consistent with the result from 2005.
4. If G-Z is indeed variable, the spread among our measurements, as well as between those from previous perihelion passages, is significantly smaller than the variation in each molecule among all comets measured (Fig. 5). This may be evidence that natal conditions dominate over evolutionary effects due to successive perihelion passages in setting the composition of short-period comets.

Understanding the cause(s) of the considerable spread of hypervolatile abundances among comets (both OCCs and short-period comets) seen in Figure 7 is necessary for disentangling primordial from evolutionary effects in setting the present-day (observed) abundances of hypervolatiles (and of primary volatiles in general) in comets. On the one hand, chemical models of protoplanetary disks (e.g., Drozdovskaya et al. 2016, Willacy et al. 2015) predict that comets incorporated a wide range of hypervolatile abundances from their formation region(s) in the protosolar nebula. On the other hand, the nontrivial effects of heterogeneous outgassing and seasonal illumination on coma composition, such as that seen by Rosetta at 67P (i.e., Bockelée-Morvan et al. 2016, Hässig et al. 2015, Luspay-Kuti et al. 2015, Fougere et al. 2016a and b, Feldman et al. 2018), cannot be overlooked. This emphasizes the high impact of serial observations of comets, particularly those targeting hypervolatiles in ecliptic comets, which may be most indicative of the role that primordial vs. evolutionary effects play in setting the composition of comets. Thankfully the availability of next-generation instruments such as iSHELL, capable of delivering the long on-source integration times and excellent sensitivity required for such measurements, is enabling us to better understand the interplay between nascent solar system conditions, evolutionary processing, and coma compositional variability when interpreting the results of primary volatile studies in comets.

Acknowledgements

Data for this study were obtained at the NASA Infrared Telescope Facility (IRTF), operated by the University of Hawai'i under contract NNH14CK55B with the National Aeronautics and Space Administration. We are most fortunate to have the opportunity to conduct observations from Maunakea, and recognize and acknowledge the very significant cultural role and reverence that the summit of Maunakea has always had within the indigenous Hawaiian community. This study was generously funded by the NASA Planetary Astronomy/Solar System Observations (NNX12AG24G, 15-SSO15_2-0028, 18-SSO18_2-0040), Planetary Atmospheres (NNX12AG60G) and Solar System Workings Programs (NNX17AC86G), the NASA Astrobiology Institute (13-13NAI7_2_0032), the NASA Emerging Worlds Program (NNN12AA01C), the National Science Foundation (AST-1616306, AST-1615441), NASA Headquarters under the NASA Earth and Space Science Fellowship Program (Grant NNX16AP49H), and International Space Science Institute Team 361. **We thank an anonymous reviewer for suggestions that improved the paper.** We acknowledge and thank the entire staff at IRTF for their support during our observations of G-Z.

References

A'Hearn, M. F. 2017, RSPTA, 375, 20160261

A'Hearn, M. F., Feaga, L. M., Keller, H. U., et al. 2012, ApJ, 758, 29

A'Hearn, M. F., Millis, R. L., Schleicher, D. G., Osip, D. J., & Birch, V. P. 1995, Icar, 118, 223

Biver, N., Bockelée-Morvan, D., Hofstadter, M., et al. 2019, A&A, 630, A19

Bockelée-Morvan, D., Crovisier, J., Erard, S., et al. 2016, MNRAS, 462, S170

Bockelée-Morvan, D., Crovisier, J., Mumma, M. J., & Weaver, H. A. 2004, in Comets II, ed. M. C. Festou, H. U. Keller, & H. A. Weaver (Tucson, AZ: Univ. of Arizona Press), 391

Bodewits, D., Farnham, T. L., A'Hearn, M. F., et al. 2014, ApJ, 786, 48

Bonev, B.P. 2005, PhD Thesis, The University of Toledo, http://astrobiology.gsfc.nasa.gov/Bonev_thesis.pdf

Bonev, B. P., Mumma, M. J., DiSanti, M. A., et al. 2006, ApJ, 653, 774

Bonev, B. P., Mumma, M. J., Radeva, Y. L., et al. 2008, ApJL, 680, L61

Bonev, B. P., Mumma, M. J., Villanueva, G. L., et al. 2007, ApjL, 661, L97

Bonev, B. P., Villanueva, G. L., DiSanti, M. A., et al. 2017, AJ, 153, 241

Cochran, A. L., Barker, E. S., & Gray, C. L. 2012, Icar, 218 144

Combi, M. R., Mäkinen, T. T., Bertaux, J. -L., Quémerais, E., & Ferron, S. 2019, Icar, 317, 610

Crovisier, J., Biver, N., Bockelée-Morvan, D., & Colom, P. 2009, P&SS, 57, 10

Dello Russo, N., DiSanti, M. A., Magee-Sauer, K., et al. 2004, Icar, 168, 186

Dello Russo, N., DiSanti, M. A., Mumma, M. J., Magee-Sauer, K., & Rettig, T. W. 1998, Icar, 135, 377

Dello Russo, N., Kawakita, H., Bonev, B. P., et al. 2019, Icar, submitted

Dello Russo, N., Kawakita, H., Vervack, R. J., Jr., & Weaver, H. A. 2016, Icar, 278, 301

DiSanti, M. A., Bonev, B. P., Dello Russo, N., et al. 2017, 154, 246

DiSanti, M. A., Bonev, B. P., Gibb, E. L., et al. 2016, ApJ, 820, 34

DiSanti, M. A., Bonev, B. P., Magee-Sauer, K., et al. 2006, ApJ, 650, 470

DiSanti, M. A., Bonev, B. P., Villanueva, G. L., et al. 2013, ApJ, 763, 1

DiSanti, M. A., Mumma, M. J., Dello Russo, N., & Magee-Sauer, K. 2001, Icar, 153, 361

DiSanti, M. A., Villanueva, G. L., Paganini, L., et al. 2014, Icar, 228, 167

Drozdovskaya, M. N., Walsh, C., van Dishoeck, E. F., et al. 2016, MNRAS, 462, 977

Faggi, S., Villanueva, G. L., Mumma, M. J., & Paganini, L. 2018, AJ, 156, 68

Feaga, L. M., A'Hearn, M. F., Farnham, T. L., et al. 2014, AJ, 147, 24

Feldman, P. D., A'Hearn, M. F., Bertaux, J. -L., et al. 2018, AJ, 155, 9

Fink, U., Doose, L., Rinaldi, G., et al. 2016, Icar, 277, 78

Fougere, N., Altwegg, K., Berthelier, J. -J., et al. 2016, A&A, 588, A134

Fougere, N., Altwegg, K., Berthelier, J. -J., et al. 2016, MNRAS, 462, 156

Gibb, E. L., Bonev, B. P., Villanueva, G. L., et al. 2012, ApJ, 750, 102

Gibb, E. L., Mumma, M. J., Dello Russo, N., et al. 2003, Icar, 165, 391

Hässig, M., Altwegg, K., Balsiger, H., et al. 2015, Science, 347 (6220), aaa0276

Kiselev, N. N., Jockers, K., Rosenbush, V. K., et al. 2000, P&SS, 48, 1005

Knight, M. M. & Schleicher, D. G. 2013, Icarus, 222, 691

Le Roy, L., Altwegg, K., Balsiger, H., et al. 2015, A&A, 583, A1

Luspay-Kuti, A., Hässig, M., Fuselier, S. A., et al. 2015, A&A, 583, A4

McKay, A. J., Cochran, A. L., DiSanti, M. A., et al. 2015, Icarus, 250, 504

Mumma, M. J. & Charnley, S. B. 2011, ARA&A, 49, 471

Mumma, M. J., DiSanti, M. A., Dello Russo, N., et al. 2000, ApJ, 531, L155

Ootsubo, T., Kawakita, H., Hamada, S., et al. 2012, ApJ, 752, 15

Paganini, L., Mumma, M. J., Boehnhardt, H., 2013, ApJ, 766, 100

Radeva, Y. L., Mumma, M. J., Bonev, B. P., et al. 2010, Icar, 206, 764

Radeva, Y. L., Mumma, M. J., Villanueva, G. L., et al. 2013, Icarus, 223, 298

Rayner, J., Bond, T., Bonnet, M., et al. 2012, Proc. SPIE, 8446, 84462C

Rayner, J., Tokunaga, A., Jaffe, D., et al. 2016, Proc. SPIE, 9908, 990884

Roth, N. X., Gibb, E. L., Bonev, B. P., et al. 2018, AJ, 156, 251

Roth, N. X., Gibb, E. L., Bonev, B. P., et al 2017, AJ, 153, 168

Stern, S. A. 2003, Nature, 424, 639

Villanueva, G. L., Mumma, M. J., Bonev, B. P., et al. 2009, ApJ, 690, L5

Villanueva, G. L., Mumma, M. J., DiSanti, M. A., et al. 2011a, Icar, 216, 227

Villanueva, G. L., Mumma, M. J., DiSanti, M. A., et al. 2012, JQSRT, 113, 202

Villanueva, G. L., Mumma, M. J., & Magee-Sauer, K. 2011b, JGRE, 116, E08012

Villanueva, G. L., Mumma, M. J., Novak, R. E., & Hewagama, T. 2008, Icar, 195, 34

Weaver, H. A., Chin, G., Bockelée-Morvan, D., et al. 1999, Icar, 142, 482

Willacy, K., Alexander, C., Ali-Dib, M., et a. 2015, SSRv, 197, 151

Figure 1. Extracted spectra of comet G-Z showing order 155 of the iSHELL Lp filter taken with the 5" long slit on UT 2018 September 11 before (left panel) and after (right panel) baseline subtraction. The gold trace is the telluric absorption model (convolved to the instrumental resolution).

Figure 2. Extracted spectra showing clear detections of CO and H_2O in comet G-Z superimposed on the cometary continuum on UT 2018 July 28. The gold trace overplotted on the uppermost cometary spectrum is the telluric absorption model (convolved to the instrumental resolution and scaled to the observed continuum level). Directly below is the residual emission spectrum (after subtracting the telluric absorption model), with the total modeled fluorescence emission overplotted in red. Individual fluorescence models (color-coded by species) are plotted below, offset vertically for clarity. At the bottom of the panel is the residual spectrum (after subtracting the telluric absorption model and all relevant molecular fluorescence models), with the 1σ uncertainty envelope overplotted in bronze.

Figure 3. A. Spatial profiles of co-measured emissions in G-Z for H_2O (black), CO (orange) and dust (red) on UT 2018 July 29. The slit was oriented along the projected Sun-comet line (position angle 223°), with the Sun-facing direction to the left as indicated. Also shown is the Sun-comet-Earth angle (phase angle, β) of 59°. The horizontal bar indicating 1″ corresponds to a projected distance of approximately 449 km at the geocentric distance of G-Z**. B.** Spatial profiles of co-measured emissions for CO (orange) and dust (red) on UT 2018 July 31. **C.** Spatial profiles of co-measured emissions for C_2H_6 (blue) and dust (red) on UT 2018 July 31. The observing geometry on July 31 was similar to that of July 29, with a position angle of 225° and a phase angle of 60°.

Figure 4. A. Extracted spectra showing detections of CO and H_2O in comet G-Z on UT 2018 July 28, with traces and labels as described in Figure 2**. B.** Detections of CH_4, C_2H_6, CH_3OH, and OH* (prompt emission) on UT 2018 July 31. The zoomed subplots highlight the locations of individual (observed and modeled) CH_4 emissions, and each subplot has the same units as the larger plot. **C.** Detections of C_2H_6, CH_3OH, and OH* on UT 2018 September 11. Analysis of CH_3OH in G-Z is the subject of a future paper. **D.** Detections of CO and H_2O on UT 2018 October 10. **E.** Detections of H_2O and OH* on UT 2018 September 7.

Figure 5. A. Comparison of mixing ratios (abundances relative to H_2O, expressed in %) of hypervolatiles in G-Z sampled on each date during the 2018 apparition. B. Comparison of mixing ratios of hypervolatiles sampled in G-Z during the 1998 apparition (purple, Weaver et al. 1999; orange, Mumma et al. 2000), 2005 (pink, DiSanti et al. 2013), and 2018 (green, yellow, cyan; this work), as well as near-infrared measurements of each volatile in OCCs (blue) and ecliptic comets (red) measured to date, and the respective mean values for CO and CH_4 among OCCs and for C_2H_6 among all comets (black, Dello Russo et al. 2016, DiSanti et al. 2017, Roth et al. 2017, Roth et al. 2018, Faggi et al. 2018, Dello Russo et al. 2019). Error bars indicate measurements with ±1σ uncertainties, whereas downward arrows indicate 3σ upper limits. **Measurements shown from 2018 are given as weighted averages for pre-perihelion and perihelion dates, and assume T_{rot} = 64 K for July, T_{rot} = 75 K for September, and T_{rot} = 60 K for October.**

Figure 6. Evolution of molecular production in G-Z throughout the 2018 perihelion passage for H_2O (left panel) and CO, CH_4, and C_2H_6 (right panel) with respect to perihelion (UT 2018 September 10). Error bars indicate measurements, whereas downward arrows indicate 3σ upper limits.

Figure 7. Abundances ratios of hypervolatiles in comets characterized to date, including comets G-Z (this work), 67P/Churyumov-Gerasimenko (Le Roy et al. 2015, Bockelée-Morvan et al. 2016, Biver et al. 2019), 45P/Honda-Mrkos-Pajdušáková (DiSanti et al. 2017), C/2006 W3 (Christensen) (Bonev et al. 2017), C/2012 K1 (PanSTARRS) (Roth et al. 2017), C/2017 E4 (Lovejoy) (Faggi et al. 2018), 2P/Encke (Roth et al. 2018), and 16 OCCs (after Dello Russo et al. 2016). **Short-period comets are highlighted with bold text, emphasizing the small number for which complete hypervolatile inventories are available.** Values for G-Z were taken from each of the three dates for which all three hypervolatiles were sampled, assuming T_{rot} = 64 K for July dates and T_{rot} = 60 K for October 10. For the October date, the downward- and leftward-facing arrows indicate the (3σ) upper limits CO/CH_4 and C_2H_6/CH_4. Due to the sensitive dependence of $Q(CH_4)$ on assumed T_{rot}, the red oval traces the total possible spread in G-Z's hypervolatile content for the range T_{rot} = 48 – 70 K. Each comet is color-coded by its mixing ratio CO/H_2O **with the exception of C/2006 W3 (Christensen), shown in pink, for which H_2O was not**

detected. [1] Values for 67P using C_2H_6/H_2O as reported in Le Roy et al. (2015) for the northern hemisphere. [2] Values for 67P using C_2H_6/H_2O as reported in Le Roy et al. (2015) for the southern hemisphere. In both cases, the blue ovals trace the total possible spread in 67P's hypervolatile content.

Table 1

Observing Log for 21P/Giacobini-Zinner

UT Date (2018)	iSHELL Setting	UT	R_h (au)	dR_h/dt (km s^{-1})	Δ (au)	$d\Delta/dt$ (km s^{-1})	T_{int} (minutes)	**Slit PA/ Length**
July 25	M2	12:02-13:58	1.20	-12.72	0.64	-13.67	85	**220°(15")**
July 28	Lp1	10:58-12:41	1.18	-12.25	0.61	-13.53	92	**222°(15")**
	M2	13:32-15:44	1.18	-12.23	0.61	-13.39	96	**222°(15")**
July 29	Lcustom	11:17-13:08	1.17	-12.07	0.61	-13.43	100	**223°(15")**
	M2	13:25-15:23	1.17	-12.06	0.61	-13.32	86	**223°(15")**
July 31	Lp1	10:42-12:56	1.16	-11.72	0.59	-13.30	120	**225°(15")**
	M2	13:50-15:24	1.16	-11.70	0.59	-13.16	74	**225°(15")**
Sept. 7	Lp1	14:01-16:14	1.01	-0.94	0.39	-1.89	54	**270°(5")**
	Lcustom	16:56-18:16	1.01	-0.90	0.39	-1.61	34	**270°(5")**
Sept. 11	Lp1	13:27-15:53	1.01	0.47	0.39	0.36	66	**271°(5")**
Oct. 10	M2	13:21-14:23	1.10	9.49	0.51	11.16	50	**276°(15")**
	Lp1	14:35-16:58	1.10	9.51	0.51	11.32	108	**276°(15")**

Notes. R_h, dR_h/dt, Δ, and $d\Delta/dt$ are heliocentric distance, heliocentric velocity, geocentric distance, and geocentric velocity, respectively, of 21P/Giacobini-Zinner, and T_{int} is total integration time on source. The slit position angle (PA) was oriented along the projected Sun-comet line on all dates. **The slit length for each date is given in parentheses. The slit width was 0.75" on all dates.**

Table 2

Hypervolatile Composition of Comet 21P/Giacobini-Zinner

iSHELL Setting	Molecule	T_{rot}[a] (K)	GF[b]	Q[c] (10^{25} mol s^{-1})	Q_x/Q_{H2O}[d] (%)
2018 July 25, R_h = 1.20 au, Δ = 0.64 au, $d\Delta/dt$ = -13.67 km s^{-1}					
M2	H_2O	(48)	1.82 ± 0.17[e]	2692 ± 292	100
	CO	(48)	(1.82)	40.5 ± 5.1	1.51 ± 0.25
	H_2O	(64)	(1.82)	3028 ± 306	100
	CO	(64)	(1.82)	47.4 ± 5.9	1.56 ± 0.25
2018 July 28, R_h = 1.18 au, Δ = 0.61 au, $d\Delta/dt$ = -13.5 km s^{-1}					
Lp1	C_2H_6	(48)	(1.91)	6.26 ± 1.28	0.23 ± 0.05
	CH_4	(48)	(1.91)	17.5 ± 4.2	0.63 ± 0.17
	C_2H_6	(64)	(1.91)	7.02 ± 1.33	0.24 ± 0.05
	CH_4	(64)	(1.91)	26.1 ± 6.2	0.88 ± 0.24
M2	H_2O	(48)	1.91 ± 0.14[e]	2771 ± 251	100
	CO	(48)	(1.91)	45.1 ± 3.6	1.63 ± 0.20
	H_2O	(64)	(1.91)	2961 ± 297	100
	CO	64^{+15}_{-11}	(1.91)	50.4 ± 4.0	1.70 ± 0.22
2018 July 29, R_h = 1.17 au, Δ = 0.61 au, $d\Delta/dt$ = -13.3 km s^{-1}					
Lcustom	H_2O	48^{+19}_{-13}	(1.97)	2643 ± 229	100
M2	H_2O	(48)	(1.97)	2527 ± 345	100
	CO	(48)	1.97 ± 0.21	34.8 ± 4.7	1.38 ± 0.26

	H_2O	(64)	(1.97)	2726 ± 369	100
	CO	(64)	(1.97)	41.2 ± 4.4	1.51 ± 0.26
2018 July 31, R_h = 1.16 au, Δ = 0.59 au, $d\Delta/dt$ = -13.2 km s^{-1}					
Lp1	C_2H_6	(48)	(1.66)	6.05 ± 0.77	0.24 ± 0.05
	CH_4	(48)	(1.66)	28.1 ± 4.1	1.12 ± 0.26
	C_2H_6	(64)	(1.66)	6.64 ± 0.94	0.24 ± 0.05
	CH_4	(64)	(1.66)	41.4 ± 6.0	1.52 ± 0.31
M2	H_2O	(48)	(1.66)	2503 ± 385	100
	CO	(48)	1.66 ± 0.22	50.1 ± 4.9	2.00 ± 0.36
	H_2O	(64)	(1.66)	2716 ± 262	100
	CO	(64)	(1.66)	58.6 ± 4.8	2.15 ± 0.27
2018 September 7, R_h = 1.01 au, Δ = 0.39 au, $d\Delta/dt$ = -1.7 km s^{-1}					
Lp1	C_2H_6	(75)	(1.8)[f]	10.6 ± 1.1	0.35 ± 0.06
	OH*	(75)	(1.8)[f]	3036 ± 357	100
Lcustom	H_2O	75 ± 3	(1.8)[f]	3206 ± 112	100
2018 September 11, R_h = 1.01 au, Δ = 0.47 au, $d\Delta/dt$ = 0.3 km s^{-1}					
Lp1	C_2H_6	66^{+12}_{-9}	(1.8)[f]	7.15 ± 0.39	0.26 ± 0.02
		(75)		7.49 ± 0.43	0.28 ± 0.02
	OH*	(75)	(1.8)[f]	2713 ± 168	100
2018 October 10, R_h = 1.10 au, Δ = 0.51 au, $d\Delta/dt$ = 11.1 km s^{-1}					
M2	H_2O	(50)	1.93 ± 0.28[e]	2054 ± 257	100
	CO	(50)	(1.93)	22.9 ± 2.9	1.11 ± 0.20
	H_2O	(60)	(1.93)	2029 ± 253	100

	CO	(60)	(1.93)	25.5 ± 3.3	1.26 ± 0.23
	H_2O	(70)	(1.93)	2028 ± 252	100
	CO	(70)	(1.93)	28.1 ± 3.2	1.39 ± 0.25
Lp1	C_2H_6	(50)	(1.93)	2.65 ± 0.42	0.13 ± 0.03
	CH_4	(50)	(1.93)	< 10 (3σ)	< 0.55 (3σ)
	C_2H_6	(60)	(1.93)	2.92 ± 0.39	0.14 ± 0.03
	CH_4	(60)	(1.93)	< 13 (3σ)	< 0.72 (3σ)
	C_2H_6	(70)	(1.93)	3.20 ± 0.41	0.16 ± 0.03
	CH_4	(70)	(1.93)	< 16 (3σ)	< 0.89 (3σ)

Notes.

[a] Rotational temperature. Values in parentheses are assumed.

[b] Growth factor. Values in parentheses are assumed.

[c] Global production rate. Uncertainties in production rate include line-by-line deviation between modeled and observed intensities and photon noise (see Bonev, 2005; Dello Russo et al. 2004; Bonev et al. 2007).

[d] Molecular abundance with respect to H_2O.

[e] Continuum (dust) growth factor.

[f] A growth factor for September dates could not be derived owing to use of the 5″ short slit; therefore, a GF of 1.8, consistent with growth factors derived for species pre- and post-perihelion, was assumed.

Table 3

Hypervolatile Abundances in 21P/Giacobini-Zinner Across Apparitions

Year	1998		2005	2018[d]				
Phase	Pre-perihelion		Pre-perihelion	Pre-perihelion	Perihelion	Post-perihelion	Mean among Comets[e]	Range in Comets[f]
CO	< 3.2[a]	10±6[b]	—	1.72±0.12	—	1.26±0.23	6.1±1.6(19)	0.30 – 26
CH_4	—	—	—	0.63 – 1.52	—	<0.55 – <0.89	0.88±0.10(19)	0.11 – 1.6
C_2H_6	< 0.08[a]	0.22±0.13[b]	0.14±0.02[c]	0.24±0.04	0.29±0.02[d]	0.14±0.03	0.55±0.08(27)	0.037 – 1.9

Notes.

Upper limits for non-detected species are 3σ. In all cases values are expressed as % relative to H_2O.

[a] Abundances taken from Weaver et al. (1999).

[b] Abundances taken from Mumma et al. (2000).

[c] Abundances taken from DiSanti et al. (2013).

[d] This work. Abundances for CO and C_2H_6 are given as weighted averages for molecules detected on multiple dates, assuming T_{rot} = 64 K for pre-perihelion values, T_{rot} = 75 K for perihelion values, and T_{rot} = 60 K for post-perihelion values. Owing to its sensitive dependence on T_{rot}, the mixing ratio for CH_4 is given as a range based on the values in Table 2. **Weighted mean values of $Q(H_2O)$ were $(2.86 \pm 0.15) \times 10^{28}$ mol s^{-1} pre-perihelion, $(3.05 \pm 0.09) \times 10^{28}$ mol s^{-1} near perihelion, and $(2.02 \pm 0.25) \times 10^{28}$ mol s^{-1} post-perihelion.**

[e] Mean values and 1σ uncertainties among measured comets taken from Dello Russo et al. (2016). The number of measurements used to calculate the mean is given in parentheses. Mean values for CO and CH_4 are given for OCCs only owing to the extreme paucity of such measurements in JFCs, whereas the mean for C_2H_6 is given for all comets measured (JFCs and OCCs).

[f] Range among comets measured after Dello Russo et al. 2016, DiSanti et al. 2017, Roth et al. 2017, Roth et al. 2018, Faggi et al. 2018, Dello Russo et al. 2019.

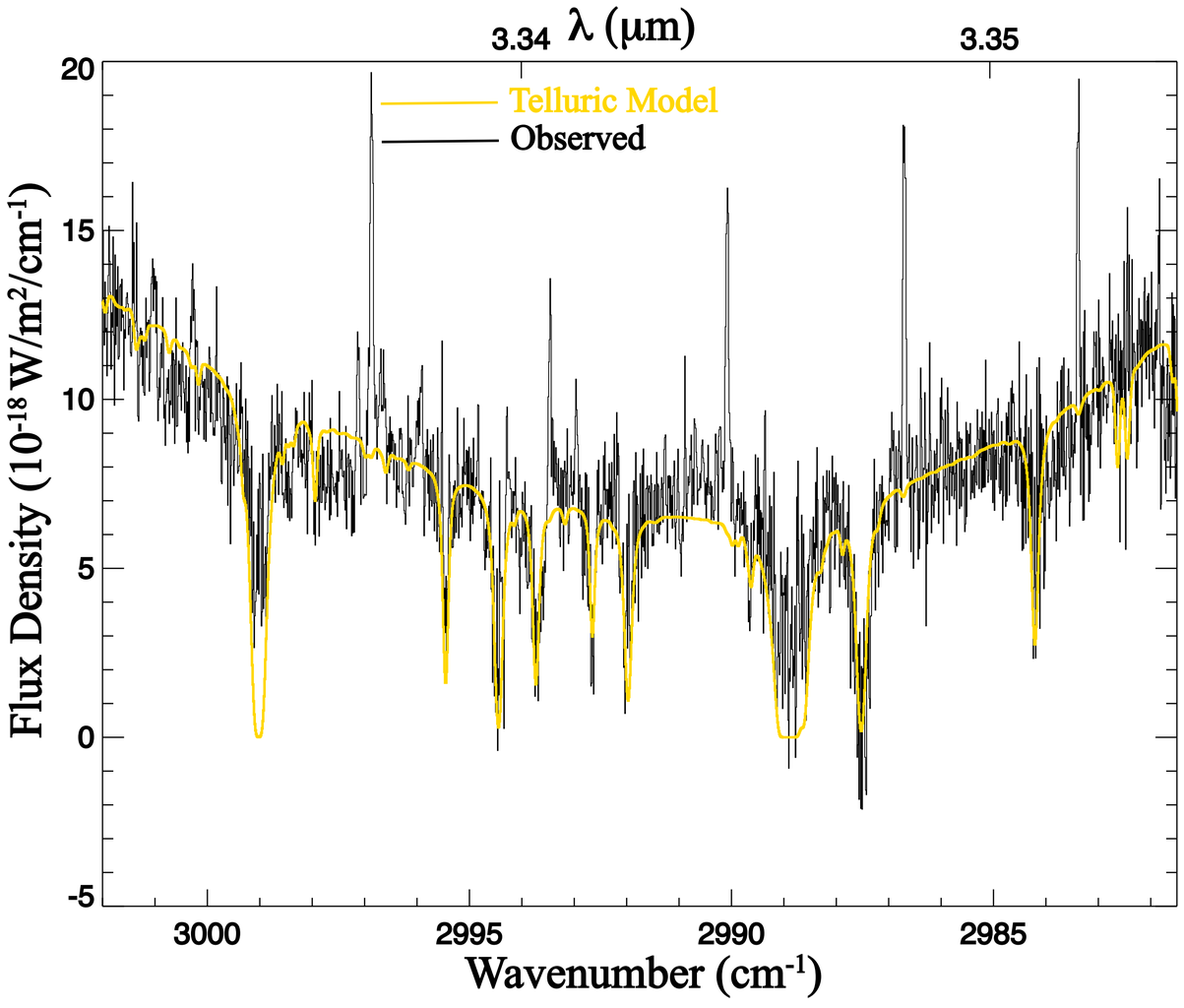
3.34 λ (μm) 3.35
Telluric Model
Observed
Flux Density (10^{-18} W/m^2/cm^{-1})
20
15
10
5
0
-5
3000
2995
2990
2985
Wavenumber (cm^{-1})

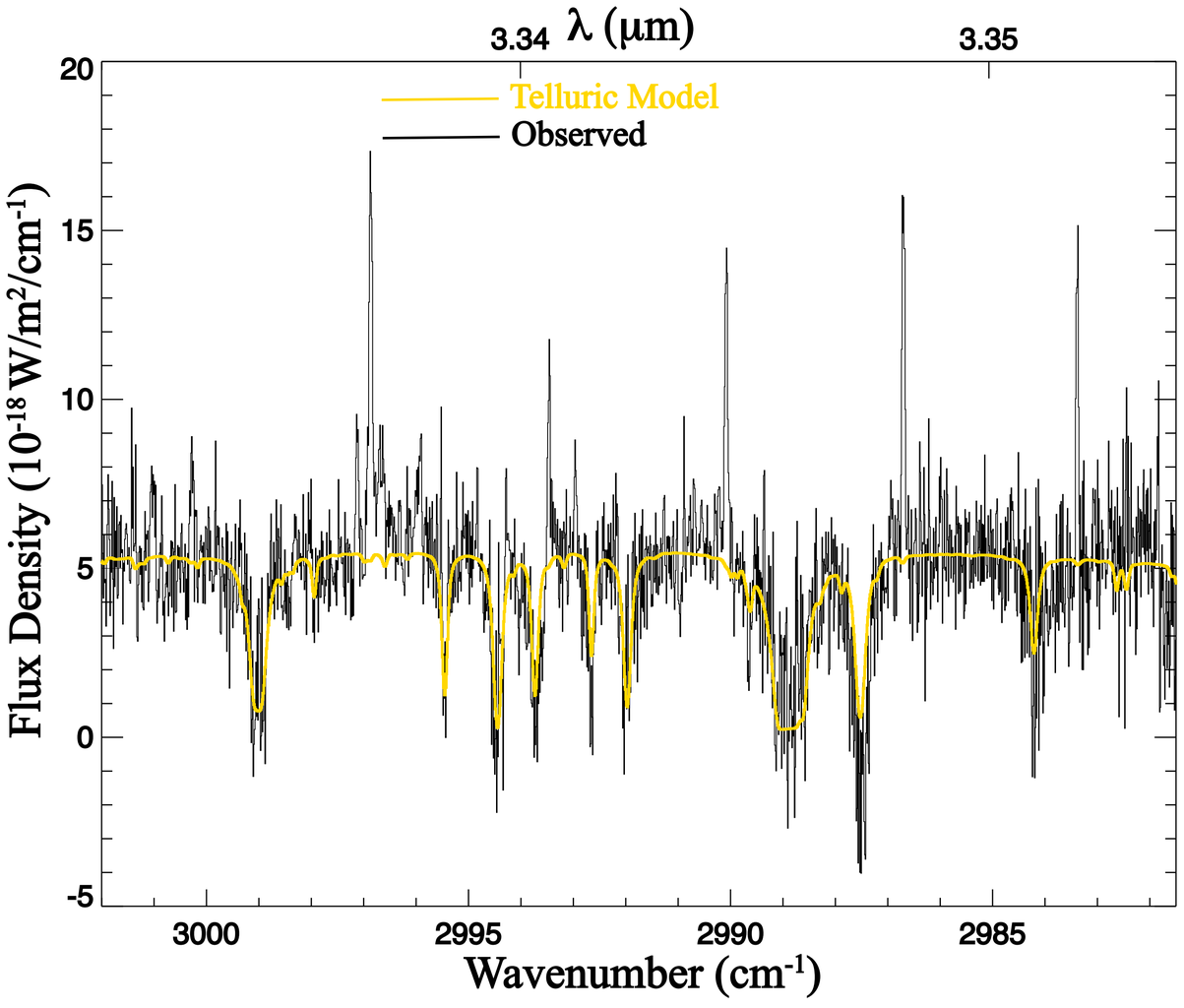
3.34 λ (μm) 3.35
Telluric Model
Observed
Flux Density (10^{-18} W/m^2/cm^{-1})
20
15
10
5
0
-5
3000
2995
2990
2985
Wavenumber (cm^{-1})

July 28

4.68 4.69 λ (μm) 4.70 4.71

5

0

Observed

Observed - Continuum

0

H_2O

CO

Observed - Continuum - Models (Residuals)

0

Flux Density (10^{-17} W/m^2/cm^{-1})

2140 2135 2130 2125

Wavenumber (cm^{-1})

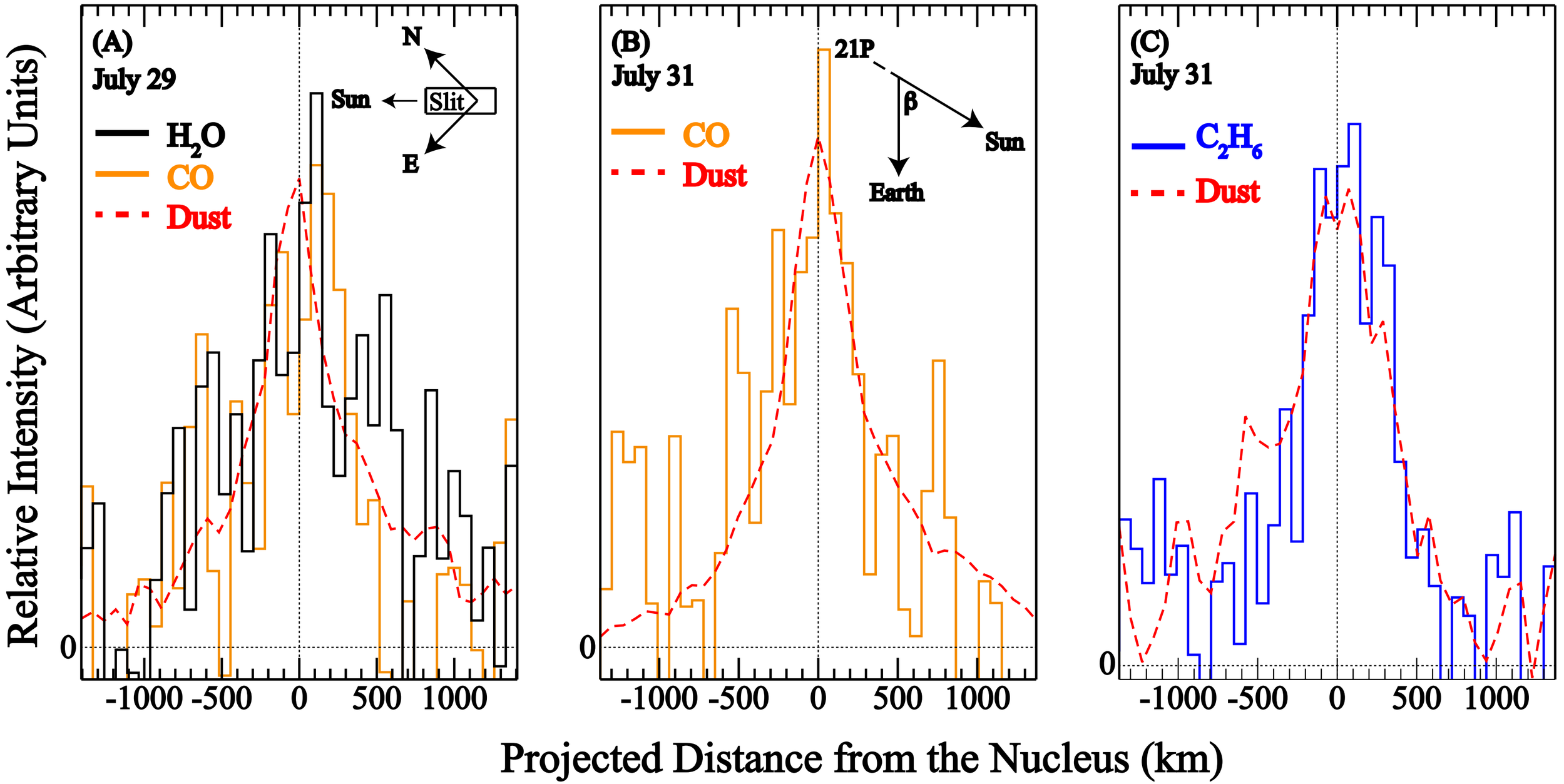
(A)
July 29
H2O
CO
Dust
N
E
Sun
Slit
(B)
July 31
CO
Dust
21P
β
Sun
Earth
(C)
July 31
C2H6
Dust
Relative Intensity (Arbitrary Units)
0
-1000
-500
0
500
1000
Projected Distance from the Nucleus (km)

July 28

4A

λ (μm)

4.64

4.65

4.66

Telluric Model

Total Fluorescence Model

Observed

H_2O

CO

Residuals

Flux Density (10^{-17} W/m^2/cm^{-1})

4

2

0

2

0

2158

2156

2154

2152

2150

2148

2146

2144

Wavenumber (cm^{-1})

July 31

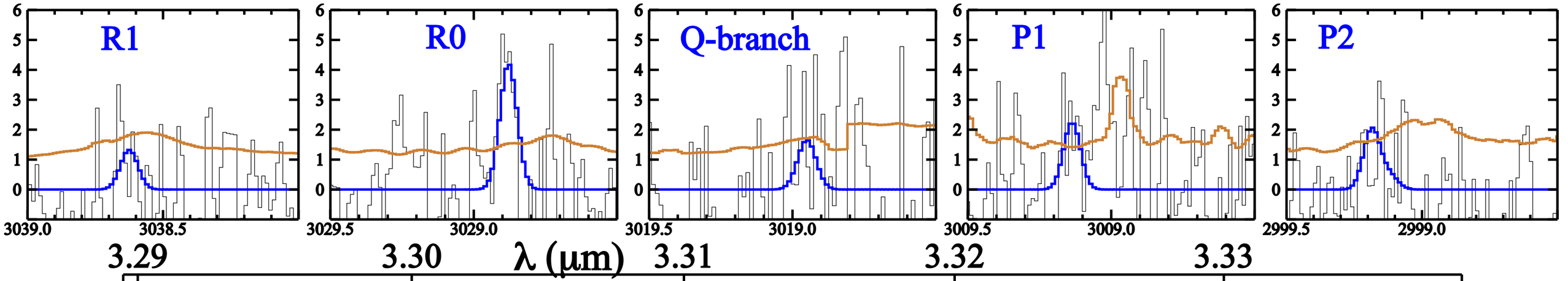
R1
R0
Q-branch
P1
P2
3039.0
3038.5
3029.5
3029.0
3019.5
3019.0
3009.5
3009.0
2999.5
2999.0

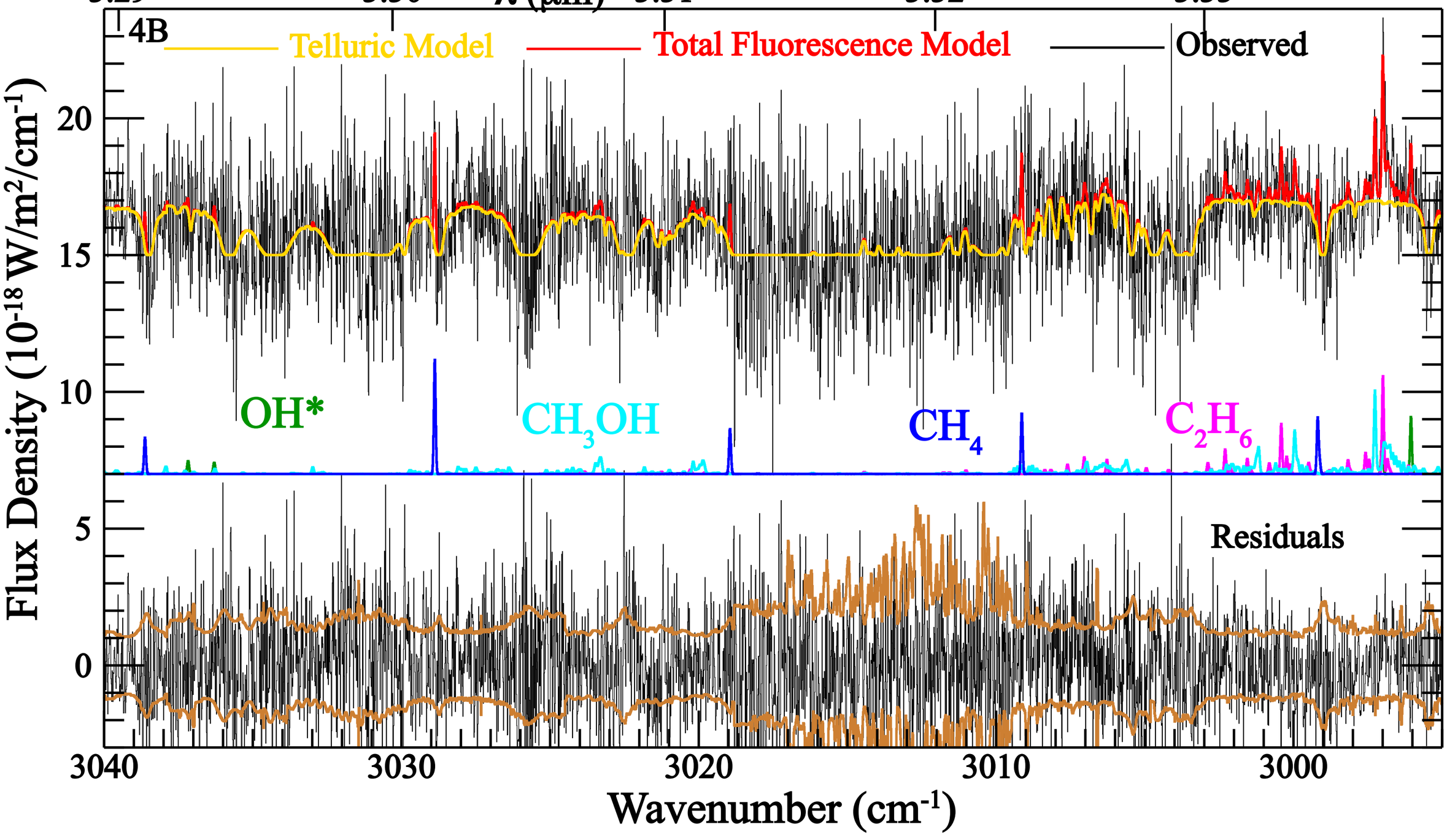
3.29
3.30
λ (μm)
3.31
3.32
3.33
4B
Telluric Model
Total Fluorescence Model
Observed
Flux Density (10-18 W/m2/cm-1)
20
15
10
5
0
OH*
CH3OH
CH4
C2H6
Residuals
3040
3030
3020
3010
3000
Wavenumber (cm-1)

September 11

3.34 λ (μm) 3.35

4C

Telluric Model

Total Fluorescence Model

Observed

CH_3OH

OH*

C_2H_6

Residuals

Flux Density (10^{-18} W/m^2/cm^{-1})

20

10

0

0

3000 2995 2990 2985

Wavenumber (cm^{-1})

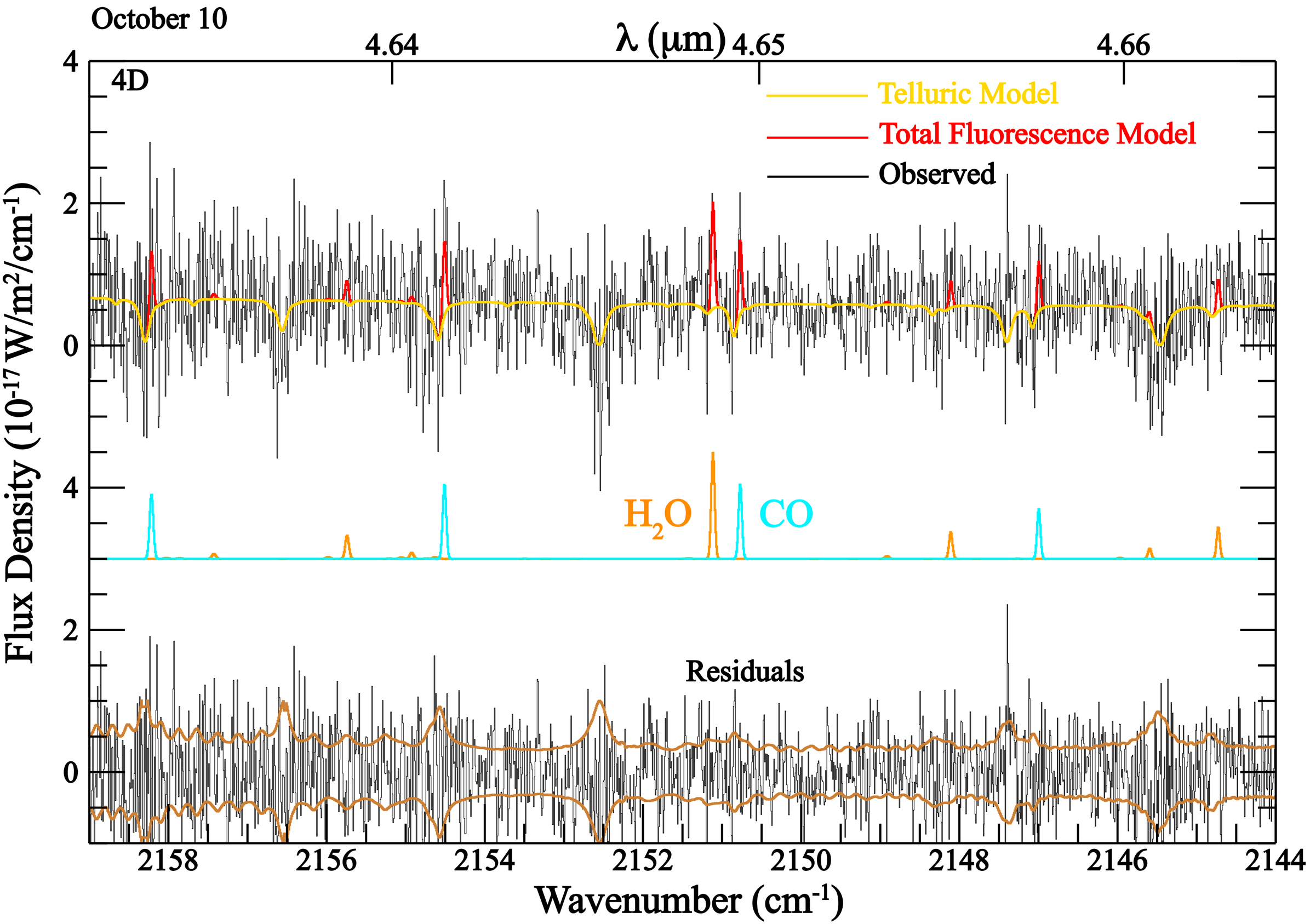
October 10
λ (μm)
4.64
4.65
4.66
4D
Telluric Model
Total Fluorescence Model
Observed
H2O
CO
Residuals
Flux Density (10-17 W/m2/cm-1)
Wavenumber (cm-1)
2158
2156
2154
2152
2150
2148
2146
2144

September 7

λ (μm)

2.89

2.90

4E

Telluric Model

Total Fluorescence Model

Observed

60

40

20

0

OH*

H_2O

Residuals

Flux Density (10^{-17} W/m^2/cm^{-1})

3465

3460

3455

3450

3445

3440

Wavenumber (cm^{-1})

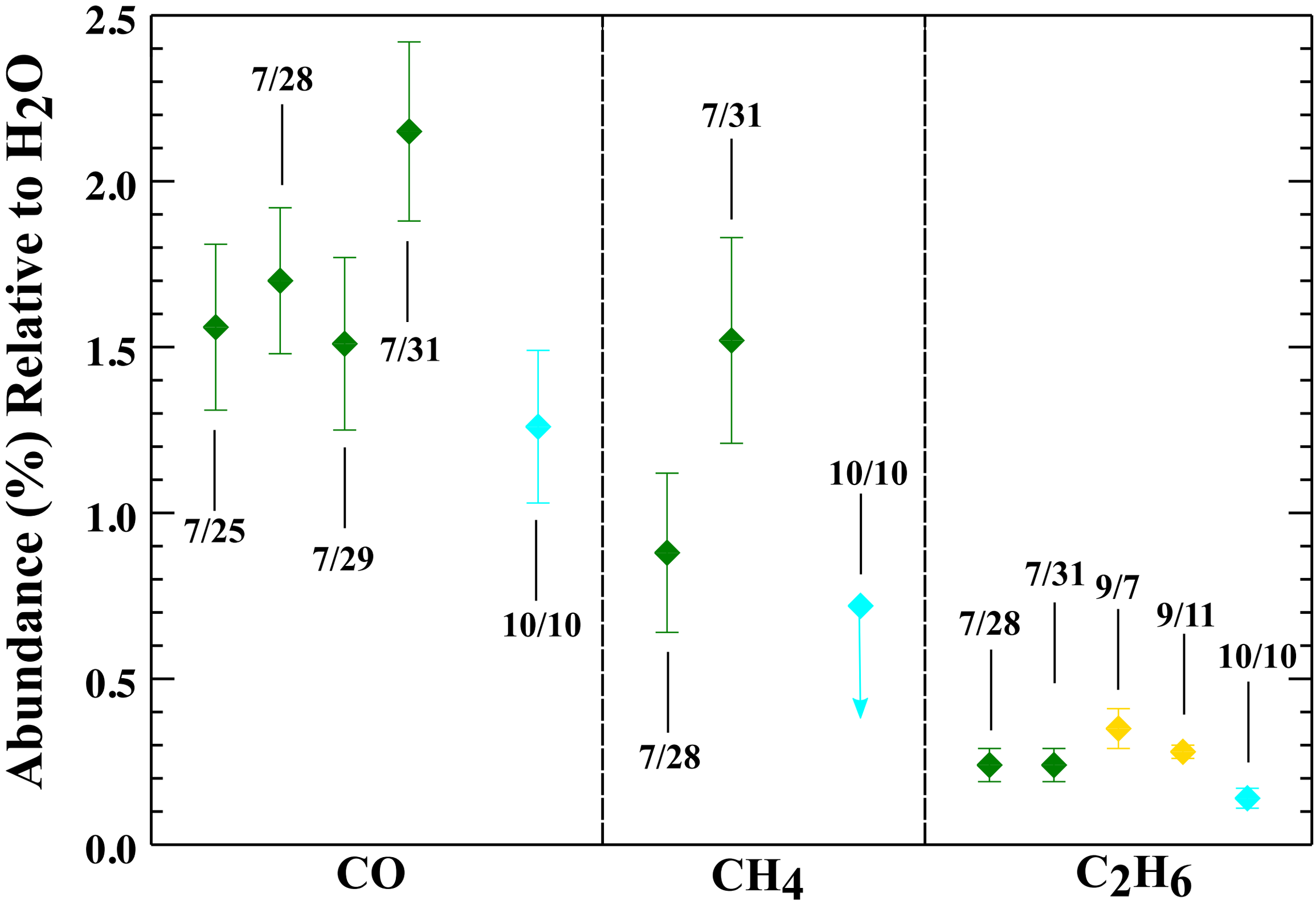
Abundance (%) Relative to H2O
2.5
2.0
1.5
1.0
0.5
0.0
7/28
7/31
7/25
7/29
10/10
7/28
7/31
10/10
7/28
7/31
9/7
9/11
10/10
CO
CH4
C2H6

GZ (1998 Apparition, Pre-perihelion)
GZ (1998 Apparition, Pre-perihelion)
GZ (2005 Apparition, Pre-perihelion)
△Oort Cloud Comets Measured to Date
△Short-period Comets Measured to Date
GZ (2018 Apparition, Pre-perihelion)
GZ (2018 Apparition, Perihelion)
GZ (2018 Apparition, Post-perihelion)
★Mean Values in Comets

Abundance (%) Relative to H_2O

10.00
1.00
0.10
0.01

CO
CH_4
C_2H_6

Evolution of Molecular Production in 21P/Giacobini-Zinner

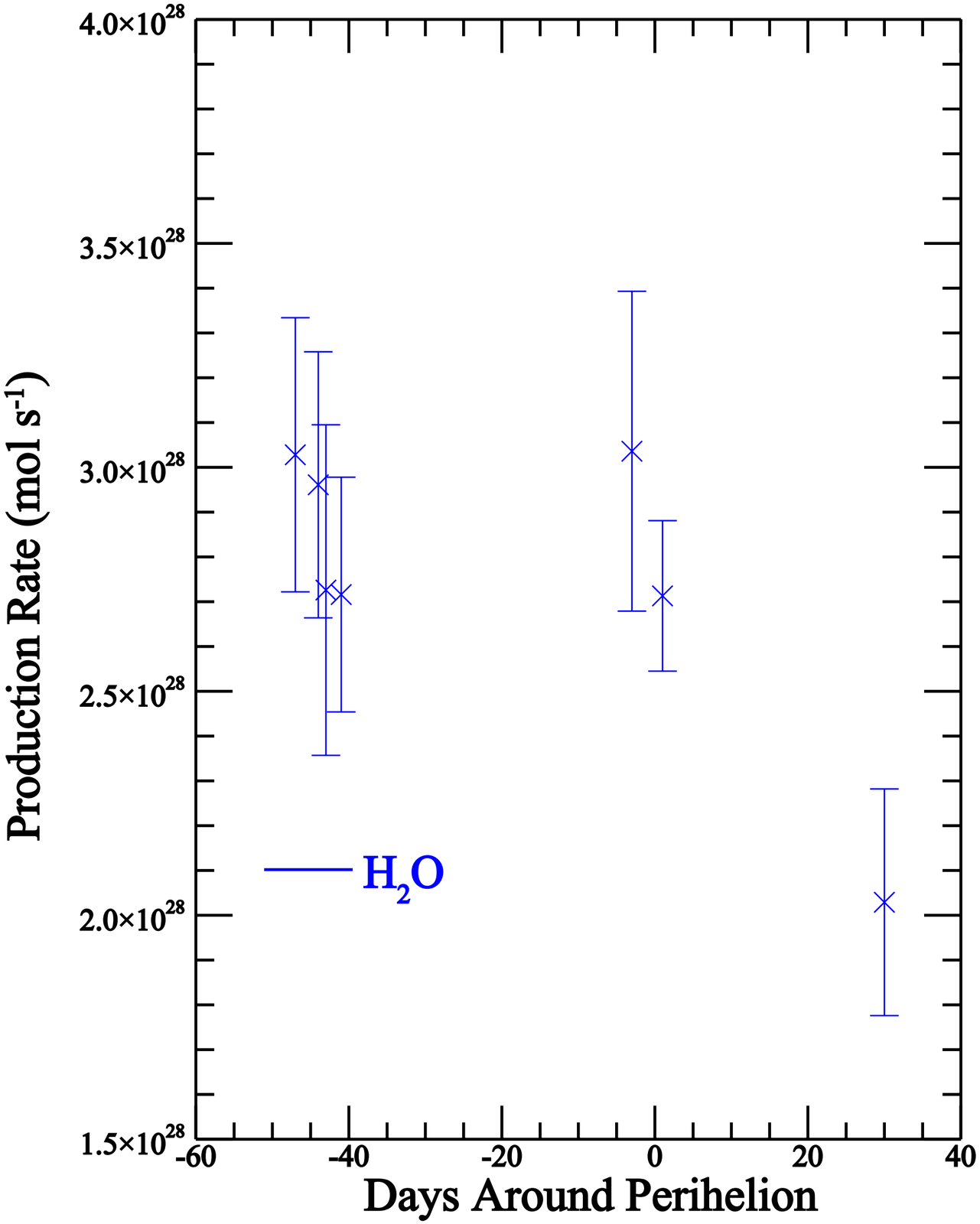

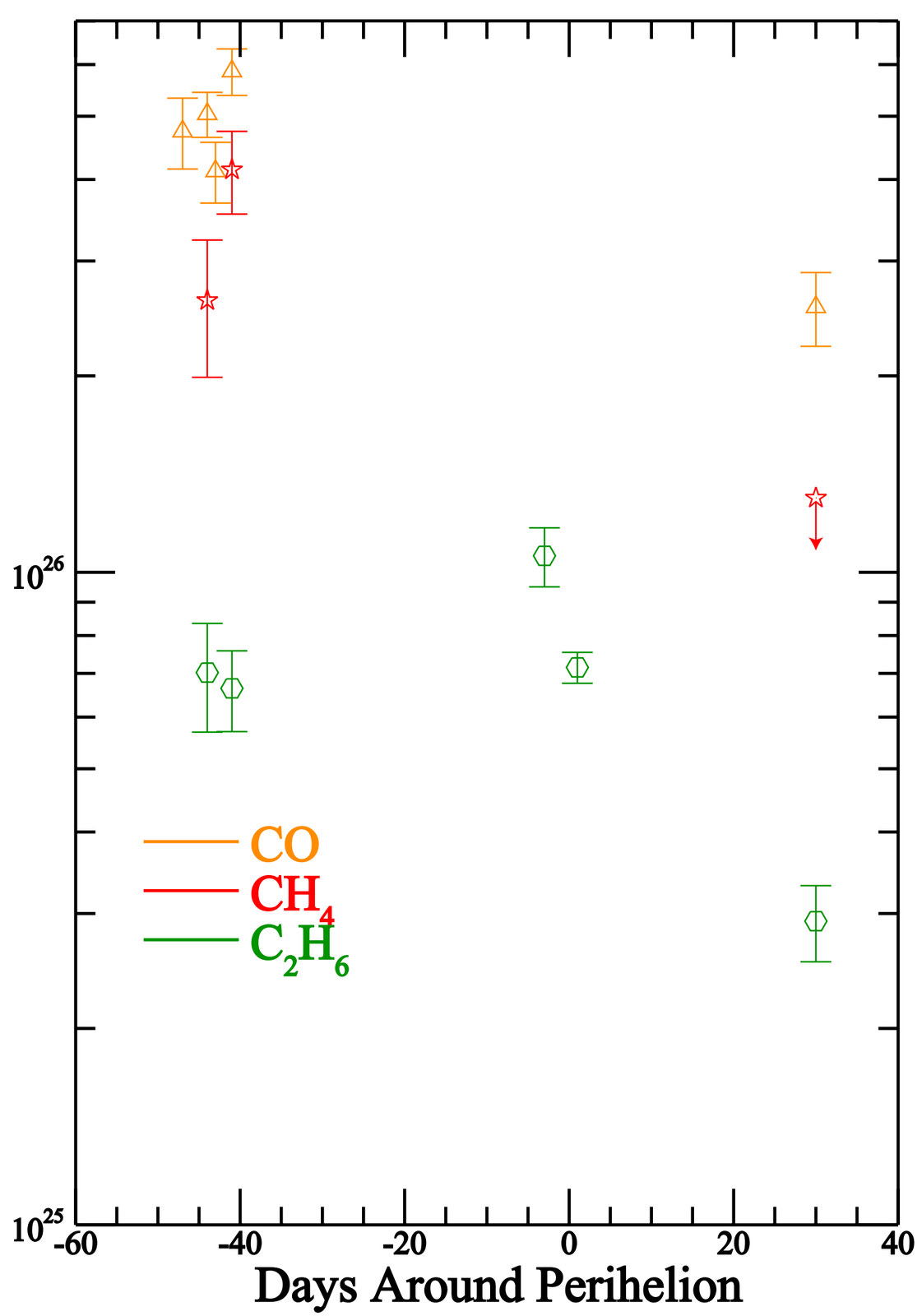

Relative Abundances of Hypervolatiles

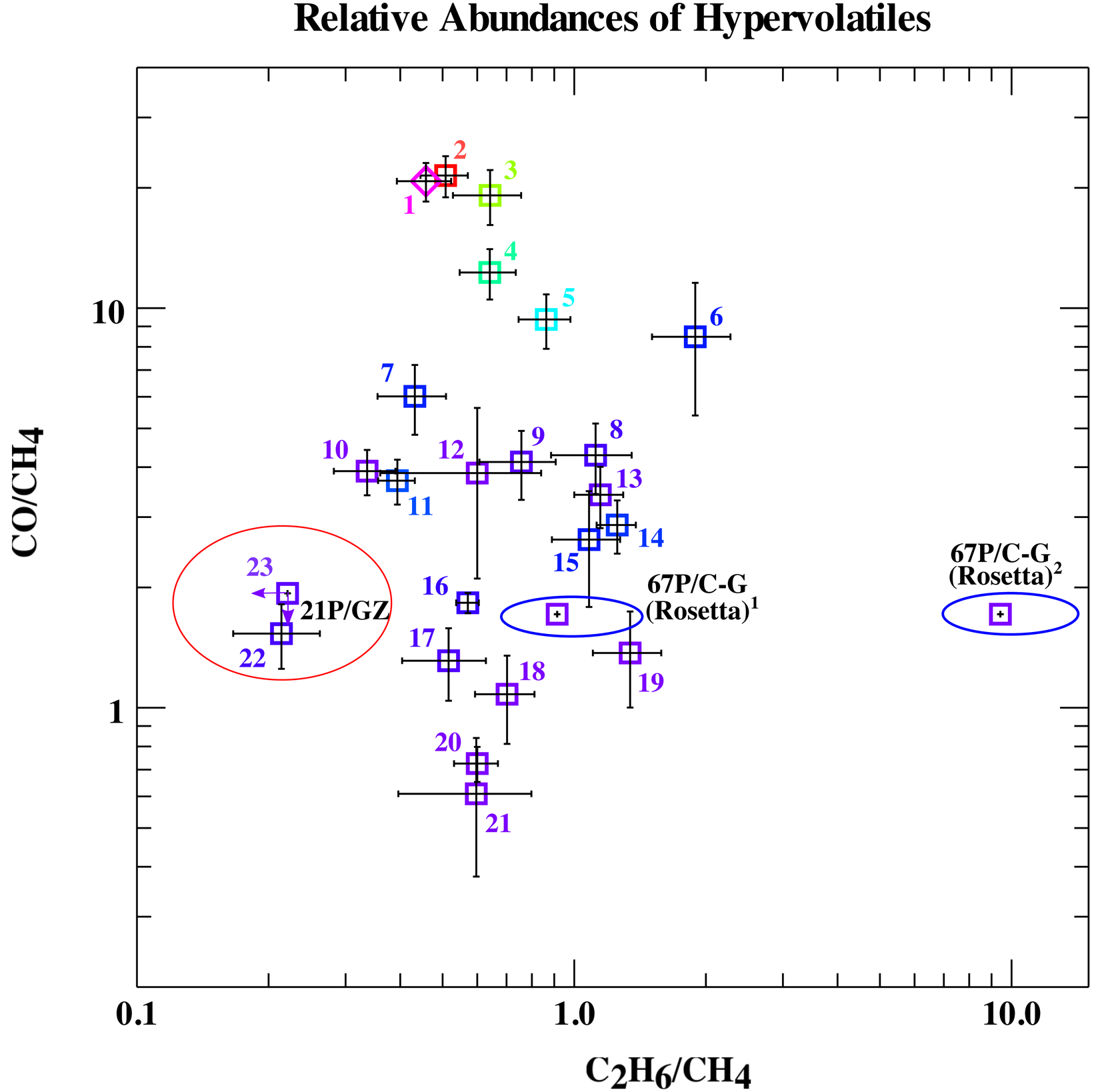

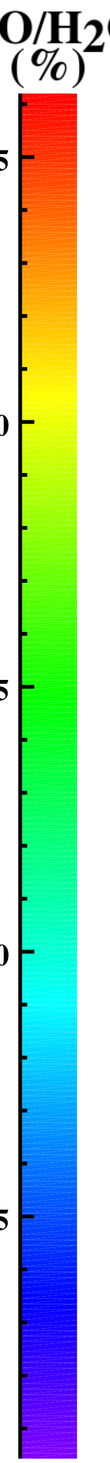

1. C/2006 W3 (Christensen)
2. C/1995 O1 (Hale-Bopp)
3. C/1996 B2 (Hyakutake)
4. C/2013 R1 (Lovejoy)
5. C/2009 P1 (Garradd)
6. C/2012 K1 (PanSTARRS)
7. C/2012 F6 (Lemmon)
8. C/2006 P1 (McNaught)
9. C/2012 S1 (ISON)
10. 2P/Encke (2017)
11. C/2004 Q2 (Machholz)
12. C/1999 S4 (LINEAR)
13. C/2017 E4 (Lovejoy)
14. C/2007 W1 (Boattini)
15. C/2001 A2 (LINEAR)
16. C/2007 N3 (Lulin)
17. C/1999 H1 (Lee)
18. 8P/Tuttle
19. C/2007 WM1 (LINEAR)
20. 45P/H-M-P
21. C/2006 M4 (SWAN)
22. 21P/G-Z (2018, Pre-perihelion)
23. 21P/G-Z (2018, Post-perihelion)